Mineralogical Diversity and Geology of Humboldt Crater Derived Using Moon Mineralogy Mapper Data

M. Martinot, S. Besse, Jessica Flahaut, C. Quantin-Nataf, L. Lozac'H, W. Van westrenen

AGU PUBLICATIONS

JGR

Journal of Geophysical Research: Planets

RESEARCH ARTICLE
10.1002/2017JE005435

Mineralogical Diversity and Geology of Humboldt Crater Derived Using Moon Mineralogy Mapper Data

M. Martinot[1,2], S. Besse[3], J. Flahaut[4], C. Quantin-Nataf[2], L. Lozac'h[2], and W. van Westrenen[1]

[1]Faculty of Science, Vrije Universiteit Amsterdam, Amsterdam, The Netherlands, [2]Université Lyon 1, ENS-Lyon, CNRS, UMR 5276 LGL-TPE, Villeurbanne, France, [3]European Space Astronomy Centre, Madrid, Spain, [4]Institut de Recherche en Astrophysique et Planétologie, CNRS/UMR 5277, Université Paul Sabatier, Toulouse, France

Key Points:
- Multiple pure crystalline plagioclase are detected in the Humboldt crater central peak complex, hinting at its crustal origin
- Olivine, spinel, and glass are detected in the crater's walls and rim, suggesting their shallow origin, possibly linked to a plutonic event
- Crater counts performed on the crater volcanic deposits suggest that volcanic activity in Humboldt crater spanned over a billion years

Supporting Information:
- Supporting Information S1
- Data Set S1

Correspondence to:
M. Martinot,
m.martinot@vu.nl

Citation:
Martinot, M., Besse, S., Flahaut, J., Quantin-Nataf, C., Lozac'h, L., & van Westrenen, W. (2018). Mineralogical diversity and geology of Humboldt crater derived using Moon Mineralogy Mapper data. *Journal of Geophysical Research: Planets*, *123*, 612–629. https://doi.org/10.1002/2017JE005435

Received 4 SEP 2017
Accepted 20 NOV 2017
Accepted article online 21 DEC 2017
Published online 26 FEB 2018

Abstract Moon Mineralogy Mapper (M^3) spectroscopic data and high-resolution imagery data sets were used to study the mineralogy and geology of the 207 km diameter Humboldt crater. Analyses of M^3 data, using a custom-made method for M^3 spectra continuum removal and spectral parameters calculation, reveal multiple pure crystalline plagioclase detections within the Humboldt crater central peak complex, hinting at its crustal origin. However, olivine, spinel, and glass are observed in the crater walls and rims, suggesting these minerals derive from shallower levels than the plagioclase of the central peak complex. High-calcium pyroxenes are detected in association with volcanic deposits emplaced on the crater's floor. Geologic mapping was performed, and the age of Humboldt crater's units was estimated from crater counts. Results suggest that volcanic activity within this floor-fractured crater spanned over a billion years. The felsic mineralogy of the central peak complex region, which presumably excavated deeper material, and the shallow mafic minerals (olivine and spinel) detected in Humboldt crater walls and rim are not in accordance with the general view of the structure of the lunar crust. Our observations can be explained by the presence of a mafic pluton emplaced in the anorthositic crust prior to the Humboldt-forming impact event. Alternatively, the excavation of Australe basin ejecta could explain the observed mineralogical detections. This highlights the importance of detailed combined mineralogical and geological remote sensing studies to assess the heterogeneity of the lunar crust.

Plain Language Summary Humboldt crater is a 207 km diameter complex impact crater located on the farside of the Moon. A central peak sits in its center, whereas its periphery is occupied by volcanic deposits. The peak was formed during the crater-forming impact event, as material from depth was brought up to the surface. In this study, we make use of the light that is reflected from the lunar surface to infer its composition. We used data from the Moon Mineralogy Mapper (M^3) instrument, a visible near-infrared spectrometer, that orbited the Moon between 2008 and 2009. We surveyed the mineralogy of the different crater units and dated them by crater counts. We found that volcanic activity in Humboldt crater might have spanned over 1 Ga. Plagioclase minerals detected in the Humboldt crater central peak hints at its crustal origin, whereas the mineralogic assemblage of the crater walls and rim is more puzzling and raises questions about the lunar crust structure.

1. Introduction

Studies of the structure of the lunar crust are important to constrain the magmatic and thermal evolution of the Moon (e.g., Shearer et al., 2006). The Lunar Magma Ocean (LMO) concept predicts that the upper part of the lunar crust was formed by floatation of plagioclase on a magma ocean, forming a >90% plagioclase-rich, anorthositic upper crust (e.g., Kaula, 1979; Warren, 1985). Denser minerals formed during the earlier stages of magma ocean crystallization (such as olivine and pyroxene) sank to the bottom the magma ocean, forming the lower crust and mantle (e.g., Lin et al., 2017; Snyder et al., 1992).

A diversity of studies using different remote sensing data have been conducted in order to establish a lunar crustal stratigraphy. Many of these focus on the mineralogical composition of the central uplift of impact craters, where material originating from greater depths is exposed (Cintala & Grieve, 1998). Scaling laws exist to estimate the depth of origin of central uplift material, which is a function of the crater's diameter (e.g., Cintala & Grieve, 1998; Melosh, 1989). Tompkins & Pieters (1999) studied the mineralogy of lunar crater's

central peaks with Clementine data, and Wieczorek and Zuber (2001) linked the results with Clementine crustal thickness models. The authors observed an increase of the mafic mineral content with depth.

More recently, studies highlighted variations in crustal composition that deviate from the global understanding of the lunar stratigraphy, pointing at the existence of significant heterogeneities within the crust. Song et al. (2013) used Lunar Reconnaissance Orbiter (LRO) Diviner data to calculate the Christiansen Feature (CF) value of lunar crater's central peaks. The CF value is an infrared emission maximum, the position of which is indicative of bulk mineralogy (Logan et al., 1973). Song et al. (2013) results pointed at the presence of lateral and vertical heterogeneities in the crustal composition. Lemelin et al. (2015) worked with the SElenological and ENgineering Explorer (SELENE) Kaguya Multiband Imager (MI) data, which provides visible near-infrared multispectral images with five spectral channels. The authors found that mafic intrusions likely intruded the lunar crust in the Feldspathic Highland Terrane and that the Procellarum KREEP Terrane and the South Pole Aitken Terrane (introduced as FHT, PKT, and SPAT by Cahill et al., 2009) impact events probably incorporated a mantle component in their melts. These results are generally consistent with the models of Head and Wilson (1992b), who proposed that buoyant diapirs of mantle might have intruded the base of the anorthositic crust during magma ocean crystallization, forming crustal heterogeneities (up to 50 % of the lower crust in volume, Head & Wilson, 1992a).

Because the material emplaced in a crater's central peak complex originates from deeper than the material observed in the crater's walls, floor, and ejecta, detailed mineralogical and geological studies of impact craters can provide constraints on local crustal structure. Here we assess the mineralogy, geology, and morphology of the Humboldt crater central peak complex, floor, walls, and rim using Moon Mineralogy Mapper (M^3) spectroscopic data, combined with high-resolution imagery data sets. We present a custom-made method to remove the continuum of M^3 spectra and to calculate spectral parameters. Our observations are aimed at shedding new light on the geology, mineralogy, and local crustal structure of the Humboldt area.

2. Humboldt Crater

Humboldt crater (27°S, 80.9°W) is a complex crater, 207 km in diameter, located on the eastern limb of the Moon. It was mapped as Upper Imbrian in age by Wilhelms and El-Baz (1977). It is surrounded by Hecataeus crater (167 km in diameter) to the north, Phillips crater (122 km in diameter) to the west, and Barnard crater (105 km in diameter) to the southeast (Figure 1a). Four volcanic deposits are emplaced on the Humboldt crater floor, identified as pyroclastic deposits possibly associated to mare ponds by Gaddis et al. (2003) (arrows in Figure 1a). The Humboldt crater floor displays numerous radial and concentric fractures (Baldwin, 1968) leading to its classification as a floor-fractured crater, interpreted to be formed by a magmatic intrusion beneath the crater floor (Schultz, 1976). The observation of vents associated with fractures on the floor of Humboldt crater by Jozwiak, Head, and Wilson (2016) supports the presence of a magmatic intrusion beneath the crater floor. The northern part of the crater floor is more hummocky than the southern part, with numerous 800 m to 2 km wide mounds, whereas the surface of the south of Humboldt crater is smoother. The mean floor altitude is −6,637 m, the mean rim altitude is −150 m, and the central peak culminates at −2,212 m. These altitudes are from the LRO Lunar Orbiter Laser Altimeter (LOLA) global elevation digital elevation model (DEM).

A line of mounds (referred to as central alignment hereafter) oriented southwest/northeast and extending from the center of the crater to the rim of the northeast pyroclastic deposit is observed (Figures 1a and 1c). The northern part of the central peak complex is connected with this central alignment, which complicates the distinction between central peak complex material and central alignment material. This central alignment has been described as a *Centralkette* (central chain) by Beer and Madler (1837) and a line of peaks by Wilhelms et al. (1987). The central peak complex of Humboldt crater is made of several elements arranged circularly (Figure 1a). Based on this observation, Baker et al. (2011) proposed that Humboldt crater is at the transition between a central peak crater and a peak ring basin.

During their global crystalline plagioclase assessment of the lunar crust, Donaldson Hanna et al. (2014) described multiple occurrences of pure crystalline plagioclase (<1% olivine and pyroxene in the rock) in the Humboldt crater central peak complex. Song et al. (2013) calculated the CF value of the Humboldt crater central peak complex and also found that it is consistent with an anorthositic composition. Yamamoto et al. (2010) detected olivine located on the floor of Humboldt crater using Kaguya Spectral Profiler (SP) data. In their study, Gaddis et al. (2003) used Clementine data to analyze the composition of lunar pyroclastic deposits.

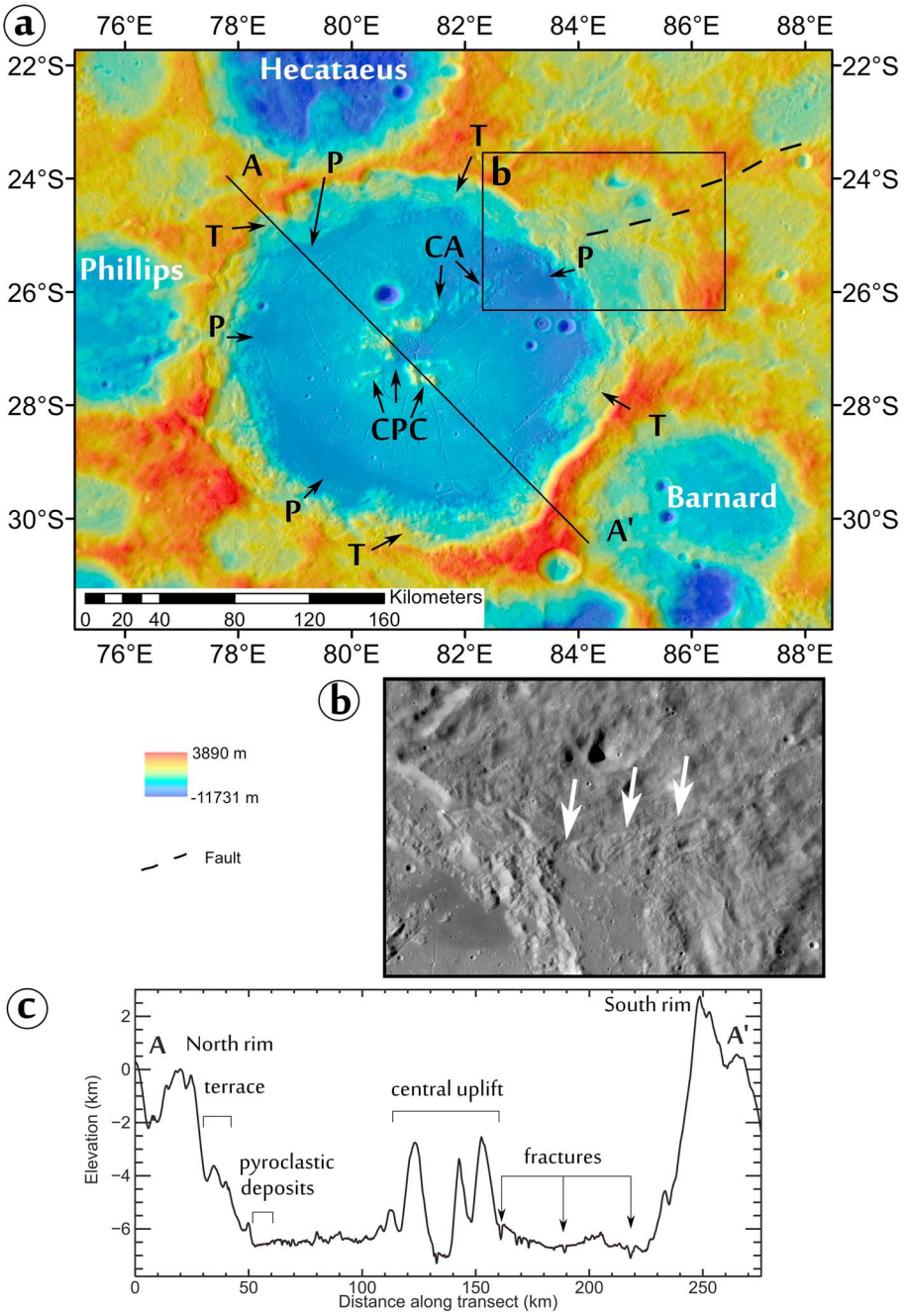

Figure 1. Geological context of Humboldt crater. (a) General view of Humboldt crater and nearby craters with a LOLA and Kaguya Terrain Camera (TC) merged DEM, overlain in transparency on a LRO Wide Angle Camera (WAC) mosaic basemap. The Humboldt central peak complex region appears in yellow shades at the center of the crater (denoted as CPC). The central alignment, denoted as CA, extends to the rim of the volcanic deposit located in the northeast portion of the crater. Volcanic deposits are located in lower elevated areas in the periphery of the crater and denoted as P. Portions of the terraced walls are marked as T. The AA′ line shows the topographic transect presented in Figures 1b and 1c. A fault of same orientation as the central alignment is observed to the northeast of Humboldt crater presented in Figure 1b. (b) Close-up of the Humboldt crater rim, where the fracture cutting the rim of the crater is denoted with white arrows. (c) LOLA/Kaguya merged DEM topographic transect AA′ of Humboldt crater. The northern rim is slightly lower in elevation than the southern rim. The crater walls are terraced. The volcanic deposits are emplaced in the topographic lows in the periphery of the crater floor.

They plotted Clementine color ratios data at 415/750 nm versus 950/750 nm and found that the Humboldt volcanic deposits plot in the uncontaminated, mature mare soils field from Staid (2000).

3. Data Sets and Methods

3.1. Remote Sensing Data

3.1.1. Moon Mineralogy Mapper

The mineralogy of Humboldt crater was derived from spectroscopic data from the Moon Mineralogy Mapper (M^3) instrument. M^3 is a hyperspectral imager that acquired visible to near-infrared data from the lunar surface between 2008 and 2009, with a spectral range spanning from 430 to 3,000 nm over 85 spectral channels (Pieters et al., 2009). The M^3 data used in this study are the calibrated data archived in the Planetary Data System (PDS, version 1 of Level 2), radiometrically corrected (Boardman et al., 2011; Green et al., 2011), thermally corrected (Clark et al., 2011), and photometrically corrected (Besse et al., 2013). The OP2C1 period of observations (spatial resolution of 280 m per pixel) was used as it provides full coverage of Humboldt crater.

3.1.2. High-Resolution Images—Lunar Reconnaissance Orbiter and Kaguya Cameras

The geologic context of Humboldt crater and its surroundings was studied with the Lunar Reconnaissance Orbiter Wide Angle Camera (LRO WAC) global map at a resolution of 100 m per pixel (Robinson et al., 2010, downloaded from the PDS). Kaguya's Terrain Camera (TC) mosaics (with a spatial resolution of 10 m per pixel) were used to obtain higher-resolution data of the Humboldt crater floor (Haruyama et al., 2008, downloaded from the SELENE data archive: http://l2db.selene.darts.isas.jaxa.jp/index.html.en).

3.1.3. Elevation Data

The Lunar Orbiter Laser Altimeter (LOLA) global Digital Elevation Model (DEM) and LOLA/SELENE TC merged stereo-derived DEMs provide elevation data with 118 and 59 m per pixel resolution at the equator, respectively (Barker et al., 2016; Smith et al., 2010). The elevation data were downloaded from the PDS.

3.1.4. Crater Counts

Crater counts were performed on TC images and WAC mosaics and used for age determination with the Craterstats 2.0 tool (Michael & Neukum, 2010, based on the method developed by Neukum, 1983. the tool is available at http://www.geo.fu-berlin.de/en/geol/fachrichtungen/planet/software/index.html), running on an Interactive Data Language (IDL) virtual machine. Only craters with diameter superior to 250 m were used for age determination. Obvious crater alignments were excluded from the crater mapping, to prevent counting secondary craters. The craters were binned with the pseudolog function provided in the Craterstats 2.0 tool (Michael & Neukum, 2010).

3.1.5. Mapping Methods

The mapping was performed on WAC images, with help from LOLA/SELENE TC merged stereo-derived DEMs and the M^3 spectroscopic data. Units were defined using the topography, mineralogy, and geomorphology of the Humboldt crater features.

3.2. Extraction of Spectral Parameters

We developed an IDL algorithm that performs a spectrum analysis on the M^3 reflectance spectra. With the routine, a continuum is automatically removed and band center locations are defined. This approach is similar to the automatic detection of band centers from Horgan et al. (2014). Horgan et al. (2014) used an upper convex hull to find the spectrum continuum, whereas in this study, linear segments connect the modeled continuum to the original spectrum in points called tie points. The algorithm maximizes the area of lunar mafic minerals and plagioclase absorption bands at 1,000 and 2,000 nm. The tie points are searched for in fixed intervals (620–1,100 nm; 1,100–1,660 nm) on a spectrum primarily smoothed with a boxcar algorithm with a width of three spectral channels in order to limit noise influence on the tie point positions. The highest wavelength tie point position is fixed at 2,700 nm. Continuum removal is performed by dividing the initial spectrum by the continuum interpolated spectrum. The two band center locations are extracted from the minimum reflectance of a fourth-order polynomial fit around the absolute minimum (400 nm interval) of the original spectrum in the corresponding band. An example of the steps followed in our routine is shown in Figure 2.

The intervals in which a search for the tie points and band centers is performed are optimized for detection of olivine, pyroxenes, and plagioclase, representing the majority of the minerals detected on the Moon. Spinel occurrences can be detected when looking at the band depth ratio, because of the peculiar shape

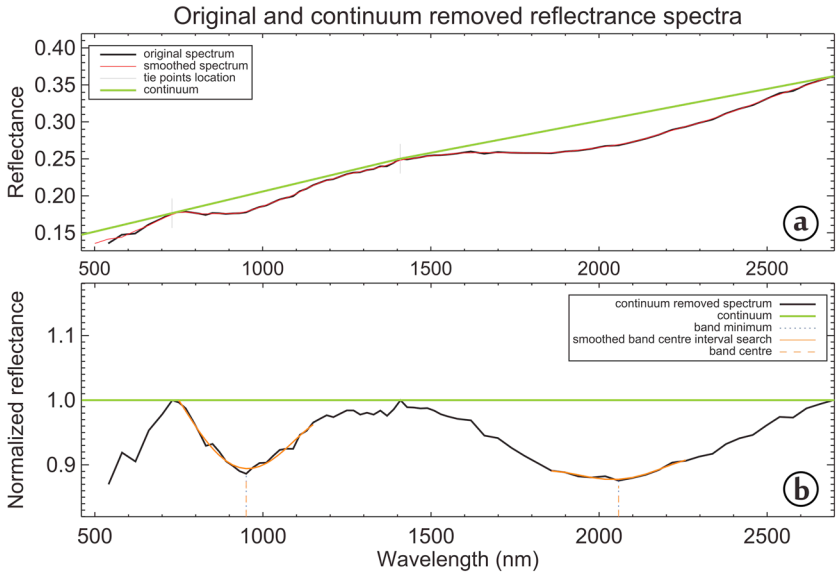

Figure 2. M^3 spectrum study with our IDL routine. (a) The original spectrum (thick black line) is smoothed (red line) to allow for the tie points search. After the tie points are found (gray vertical segments), the continuum is modeled as linear segments between the tie points (green lines). (b) Spectrum after continuum removal (thick black line). After the band minima are found (dotted blue lines), a polynomial fit (orange curve) ±200 nm around the band minimum is performed. The minimum of this polynomial fit is the band center (dashed orange line).

of its reflectance spectrum (presence of a single absorption band around 2,000 nm). Reflectance data at wavelengths lower than 620 nm were not considered because of the low signal-to-noise ratio recovered in this part of the spectrum (Green et al., 2011). The M^3 spectral domain stops at 3,000 nm, preventing a correct assessment of the thermal contribution of the lunar surface (Clark et al., 2011). Owing to this problem, reflectance data at wavelengths beyond 2,700 nm were not considered. Moreover, Pieters et al. (2009) discovered hydroxyl and water signatures in lunar spectra at these high wavelengths that can significantly affect the location of the tie points.

After removing the continuum from the spectrum, a number of spectral parameters were derived or calculated for each spectrum (Table 1). This spectrum study is repeated on each pixel of the M^3 mosaic, and several data

Table 1
List of the Spectral Parameters Calculated on the Continuum-Removed Spectrum Generated by Our IDL Routine

Parameter	Notation	Definition
Tie point 1	TP1	Position of the first tie point
Tie point 2	TP2	Position of the second tie point
Band minimum	B_nMIN	Position of the lowest value of the spectrum between two tie points
Band center	B_nCEN	Position of the minimum of a fitted 4th degree polynomial, ±200 nm from the band minimum
Band depth	BD_n	1 — the reflectance value of the band center
Band area	B_nAREA	The sum of the band depth of each spectral channel in the absorption band multiplied by the spectral resolution
Band asymmetry	B_nASYM	Percentage of difference between the area at the left and at the right of the band center, divided by the band area
Interband distance	INTERD	Difference between the position of the band center of the 1,000 and the 2,000 nm absorption band

Note. n equals 1 for the 1 μm absorption band, or 2 for the 2 μm absorption band.

products are extracted: a continuum-removed mosaic is generated, as well as spectral parameter mosaics, where all the spectral parameters calculated are stored as maps.

The parameter maps are then refined using filters to remove noise: all the pixels with a band depth less than 2% are not displayed. Filtered parameter maps are used to make color composites and stretched using ENVI to highlight pixels displaying spectral characteristics inherent to lunar mineralogy. For instance, the asymmetry of the 1 μm band can help highlight olivine, and the ratio between the 1 and 2 μm band area highlights spinel. The position of the center of the 2 μm band helps differentiating the different pyroxene groups, while olivine and plagioclase are distinguished by the position of the center of the 1 μm band. The spectra corresponding to the displayed pixels are then manually checked and compared to relevant laboratory spectra (e.g., absorption band center, band asymmetry, and shoulders position) in order to confirm or reject a mineralogical detection. The color composites are then imported in a GIS software and compared with other existing data sets. These include the global mosaic of the LRO WAC to visualize the geological context, the LOLA/SELENE TC merged stereo-derived DEM to provide elevation informations, and Kaguya TC mosaics to yield high-resolution images.

4. Results

4.1. Mineralogical Detections

Burns (1993) showed that minor amounts of FeO (<1.0 wt %) can be incorporated in lunar calcic plagioclase. Iron-bearing plagioclase is characterized by a diagnostic absorption band centered at 1,250 nm (Adams & Goullaud, 1978). However, as Cheek. et al. (2009) pointed out, olivine and pyroxene absorption bands dominate the near-infrared spectra. In a plagioclase-dominated mixture, as little as 2 vol% of olivine or pyroxene has a strong effect on the bulk spectrum (Cheek & Pieters, 2014), to the extent that plagioclase would not be identifiable in the spectra. Therefore, detecting plagioclase with near-infrared spectra provides a constraint on the plagioclase content of the rock to be superior or equal to 98% (Cheek et al., 2013; Donaldson Hanna et al., 2014; Ohtake et al., 2009). In the selected color composite shown in Figures 3a and 3b, plagioclase detections are highlighted in colors from blue to pink, with increasing absorption band strength. Plagioclase is widely detected across the central peak complex of Humboldt crater (Figure 3b), therefore suggesting the presence of nearly pure anorthosites. Figure 3c gives an example of a typical plagioclase spectrum detected in the central peak complex of Humboldt crater. No pure crystalline plagioclase is detected on the central alignment.

Olivine spectra are characterized by a single, broad and complex absorption band centered at 1,050 nm (Sunshine & Pieters, 1998). The position of the absorption center shifts toward longer wavelength with increasing iron content (Burns, 1970), and the absorption band of fayalite is broader and more flat-bottomed than that of forsterite (Sunshine & Pieters, 1998). Olivine is displayed in red in the color composite shown in Figure 3a. Olivine is mostly detected in the southern and eastern rims and ejecta of Humboldt crater, and in the walls of a 7 km diameter crater to the east of Humboldt crater's central peak complex. One olivine occurrence is observed on the western margin of the central peak complex of Humboldt crater, associated with a glass detection. All the olivine spectra observed in Humboldt crater have a narrow absorption band, and the right shoulder of the absorption band is compatible with a forsteritic composition. No compositional difference is observed between the walls and the central peak complex olivine spectra.

Pyroxenes have diagnostic absorption bands located around 1,000 and 2,000 nm, shifting toward longer wavelengths with increasing iron or calcium content (Klima et al., 2007). Low-calcium pyroxene (LCP) such as pigeonite has an absorption band centered around 900 nm and an absorption band centered around 2,000 nm. In contrast, high-calcium pyroxene (HCP) such as augite or diopside has absorption bands shifted toward longer wavelengths, around 1,000 nm and 2,200 to 2,300 nm (Adams, 1974). The color composite presented in Figure 3 displays pyroxenes in green to yellow depending on the strength of the absorption bands. HCP occurrences are associated with the volcanic deposits and ejecta of Humboldt crater, while the pyroxene detections associated with the walls of Humboldt crater, part of the central alignment, and small craters on its southwest and southeast rim, have spectral characteristics consistent with a LCP composition (e.g., pigeonite).

Small spinel patches (≤1 km in diameter) can be detected in Humboldt crater, mainly concentrated in the eastern part of its walls, rim, and ejecta (see Figure 3a). Spinel does not display any absorption feature around 1,000 nm but shows a broad absorption band centered at 2,000 nm (Cloutis et al., 2004).

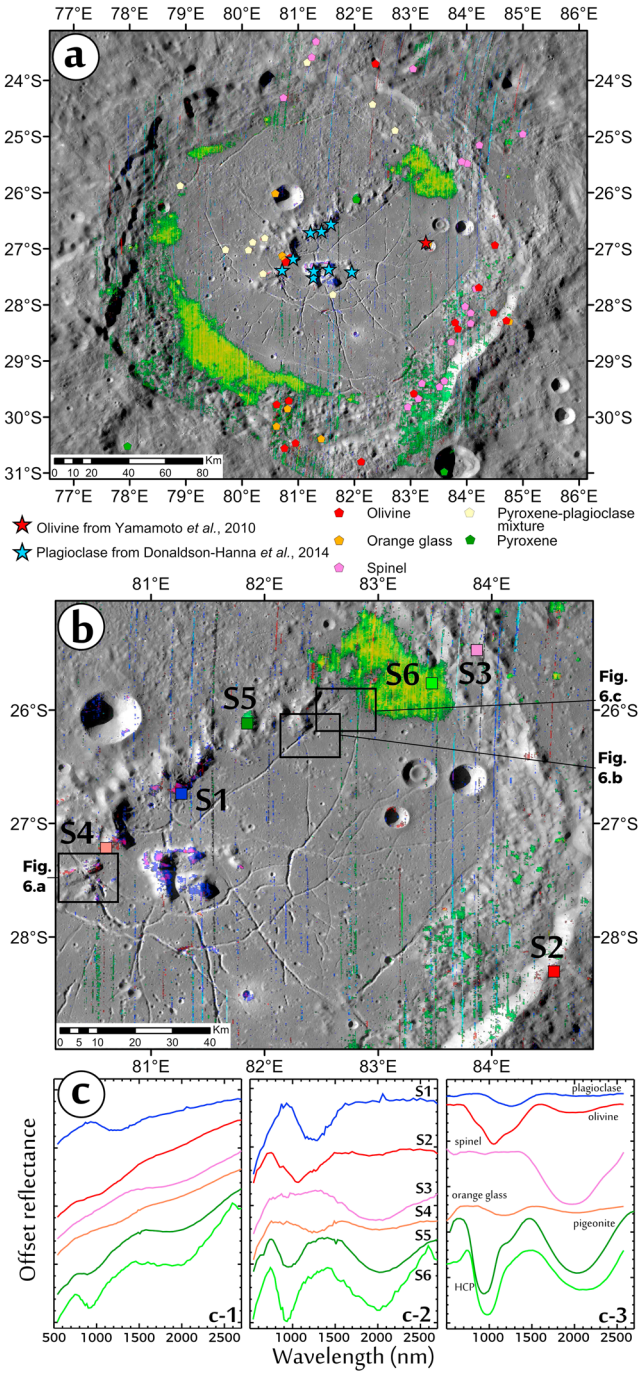

Figure 3. Humboldt crater mineralogical diversity. (a) General view of Humboldt crater with mineralogical detections. The M^3 color composite is overlain on LRO WAC mosaic. R = B1AREA; G = B2AREA; B *I* = B1CEN, see Table 1 for parameter details. Plagioclase is highlighted in blue to pink shades, as its absorption band depth increases. Olivine is displayed in red, and pyroxene in bright green. Blue stars denote pure plagioclase detections from Donaldson Hanna et al. (2014); the red star denotes the olivine detection by Yamamoto et al. (2010). The mineralogical detections from this study are reported as pentagons. The spectra associated with the light yellow pentagons are interpreted as pyroxene-plagioclase mixture spectra, as discussed in section 4.1. (b) Close-up of the Humboldt crater central peak complex and central alignment. The position of the spectra presented in Figure 3c are indicated as colored squares, and the frames are the locations of the areas shown in higher resolution in Figure 6. (c) Typical M^3 spectra of key mineralogical detections in Humboldt crater as indicated by colored squares in Figure 3b. c-1: original M^3 Level 2 spectra; c-2: continuum-removed spectra, output from the IDL routine; c-3: corresponding RELAB database spectra processed by the IDL routine (respective RELAB-ID: LS-CMP-004, LR-CMP-014, PS-TXH-082, LR-CMP-051, DL-CMP-008, and LS-CMP-009 for plagioclase, olivine, spinel, orange glass, pigeonite, and high-calcium pyroxene).

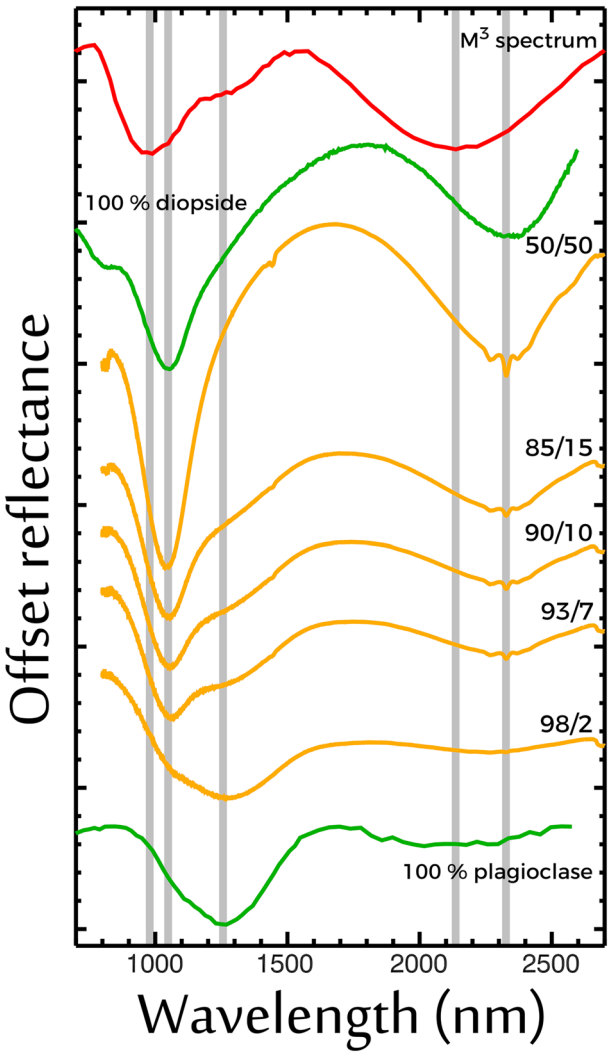

Figure 4. RELAB diospide and plagioclase mixture spectra and a M^3 spectrum. From top to bottom: M^3 spectrum collected on Humboldt crater, pure diopside spectrum (PD-CMP-008), laboratory mixture of 50% plagioclase and 50% diopside (MX-CMP-104-C), laboratory mixture of 85% plagioclase and 15% diopside (MX-CMP-102-C), laboratory mixture of 90% plagioclase and 10% diopside (MX-CMP-101-C), laboratory mixture of 93% plagioclase and 7% diopside (MX-CMP-100-C), laboratory mixture of 98% plagioclase and 2% diopside (MX-CMP-098-C), and pure plagioclase spectrum (LS-CMP-004). The spectra RELAB-ID are given in parentheses. The gray lines represent the spectra absorption band centers.

Orange glass occurrences are highlighted in red to dark red patches in the color composite (Figure 3a). Orange glass is defined by broad 1,000 nm and 2,000 nm absorption features, with centers located near 1,150 nm and 1,900 nm (Adams et al., 1974) (Figure 3c). Volcanic glass has been detected from orbit several times (Besse et al., 2014; Horgan et al., 2014; Mustard et al., 2011). Several detections of orange glass are observed spatially close to olivine on the rim and ejecta of Humboldt crater, in and near its central peak complex, and in the walls of smaller craters on its floor (see Figure 3c). Horgan et al. (2014) cautioned about the effect of Fe-bearing glass on resulting reflectance spectra when mixed with pyroxene. They showed that when glass is less abundant than 80 wt % in a glass-pyroxene mixture, the resulting spectrum mimics the spectral characteristics of olivine. When spatially detected close to one another, olivine and glass occurrences should therefore be considered with caution.

In addition, some spectra with a composite 1,000 nm absorption feature were observed on the crater floor and walls (white polygons in Figure 3a). These spectra have three absorption band centers: one at 970 nm, one at 2,020 nm, and a third at 1,230 nm (red spectrum in Figure 4). Plagioclase-diopside mixture spectra from the RELAB database (http://www.planetary.brown.edu/relab/) are shown in Figure 4. The plagioclase-diopside mixture spectra containing 7 and 10% of diospide both have an absorption feature centered at 1,250 nm additional to the 1,000 and 2,000 nm absorption features.

There is a shift in the 1 and 2 μm absorption band centers of the laboratory spectra and the spectra from the M^3 data presented here. This shift can be caused by a compositional difference: the HCP pyroxene group includes a variety of compositions that translates into spectral changes (band centers and shoulders). Figure 4 highlights the composite shape of the absorption band at 1 μm of the mixed laboratory spectra. Taken together, these elements suggest that the locations of spectra denoted by white polygons in Figure 1a may be characterized by a mixture of plagioclase and pyroxene. A possible explanation for the observation of these spectra close to the volcanic deposits and floor fractures is the mixture between HCP and plagioclase. However, some of these mixture spectra are located spatially far from the volcanic deposits, in the walls and in the central peak complex of Humboldt crater. These could be caused by the mixture between plagioclase and a pyroxene of a different composition, brought up by the impacting event.

4.2. Scatterplots

The calculation of spectral parameters for each pixel of the M^3 mosaic enables the use of scatterplots, similar to Horgan et al. (2014). Figure 5a presents a scatterplot of the values of the 1 μm band center as a function of the values of the 2 μm band center. The boxes represent fields of band center combinations compatible with the spectral parameters of a mineral. If a spectrum displays a pair of 1 and 2 μm band centers with values consistent with one of the boxes, its pixel is highlighted in Figures 5b and 5c. The values bounding the fields are those used by Horgan et al. (2014). Figure 5b shows the results of the scatterplot on the map, and Figure 5c presents a zoomed-in view of the Humboldt crater central peak complex. Several vertical stripes of pixels are highlighted, which can be explained by the residual noise left after the M^3 radiometric calibration. When located along these strips, only pixel patches larger than the width of these strips were considered in the spectral analysis. However, we find some correlations between Figure 5b and the detections presented in Figures 3a and 3b. The pixels highlighted in green in Figure 5b are the ones with spectra having clinopyroxene-compatible band 1 and 2 μm centers (e.g., pigeonite and augite). This clinopyroxene-compatible signature is in good agreement with the pyroxene signature highlighted in green

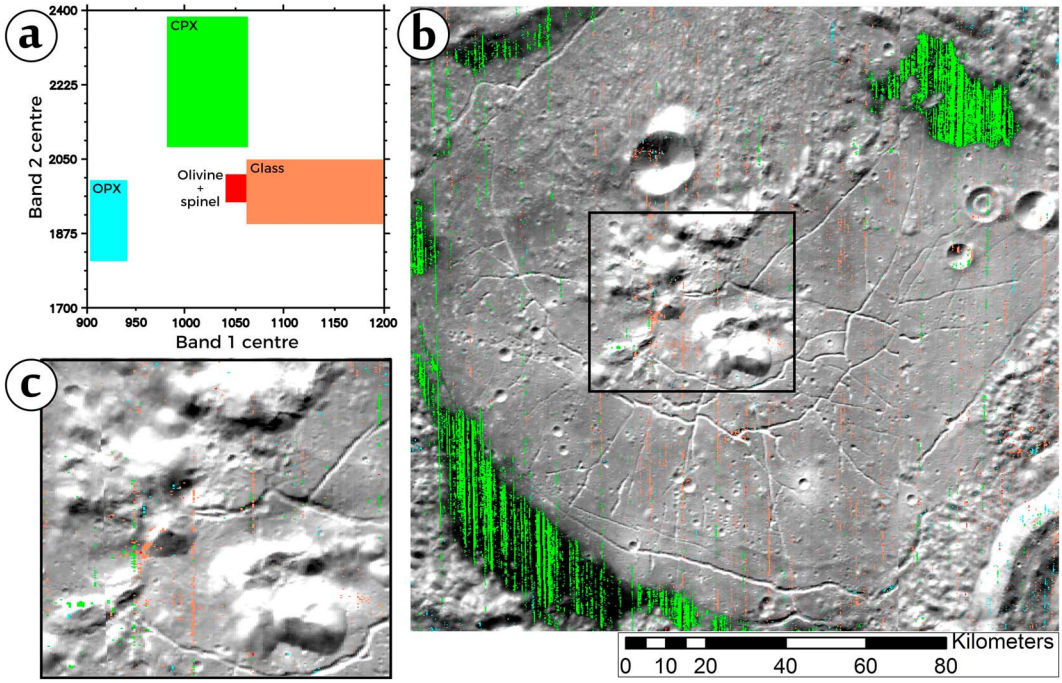

Figure 5. (a) Scatterplot presenting the values of the 1 μm band center as a function of the values of the 2 μm band center for the pixels of the M^3 mosaic of Humboldt crater. The drawn boxes represent the field of possible band centers for describing a given mineral (green for clinopyroxene, cyan for orthopyroxene, orange for glass, and red for olivine with spinel). The pixels falling within the field have spectra exhibiting the combination of band centers and are colored in Figures 5b and 5c. The values used for the absorption band centers are those used by Horgan et al. (2014). (b) M^3 2,900 nm band image of the Humboldt crater. The colored pixels are the pixels which 1 μm band center and 2 μm band center values fall in the boxes drawn in Figure 5a. (c) Close-up of the Humboldt crater central peak complex.

in the color composite (Figures 3a and 3b). Orange pixels represent pixels with spectral band 1 and 2 μm centers compatible with a glass signature. Although the results presented in Figures 5b and 5c are noisy, some locations of highlighted pixels are the same as the glass detections indicated as orange polygons in Figure 3. There was no mineral field for plagioclase in Figure 5a, but the fact that the central peak complex pixels are not highlighted is consistent with their plagioclase signature, shown Figures 3a and 3b.

4.3. Crater Morphology

Different geomorphological units can be observed on the Humboldt crater floor. The northern crater rim is lower in elevation than the southern rim. The transect shown in Figure 1c cuts through one of the volcanic deposits. Several slumps can be observed around the crater, forming wall terraces (marked as T in Figure 1a). The Humboldt crater's central peak complex is made of several blocks organized irregularly around the center of the crater. A central alignment is extending from the northwestern portion of the central peak complex to the rim of the volcanic deposit in the northeast of Humboldt crater.

Floor fractures cut through the least elevated parts of the central peak complex (Figure 6a) and central alignment (Figure 6b), which suggests that these fractures are younger than the central peak complex and central alignment. In the periphery of the crater, the fractures are covered by volcanic deposits (Figure 6c), stratigraphically constraining the age of the volcanic deposits to be younger than the fractures.

4.4. Crater Counts

Absolute ages estimated from crater counts were obtained for various units of Humboldt crater. Crater counts were performed on the northern rugged floor unit, the southern smooth floor unit, all four of the volcanic deposits, as well as a melt pool located on Humboldt proximal ejecta, to the east of the crater (see Figure 7 and supporting information for locations and age results). The northern crater floor unit exhibits a large crater proportional to the unit surface. The ejecta of this large crater cover the crater floor surface, which biases the age of the surface. In order to prevent this age bias, this large crater and ejectas were excluded from the crater counts. The age results were obtained with the production and chronology functions from Neukum et al. (2001). The crater counts of volcanic deposits were performed on TC images. Only the craters with

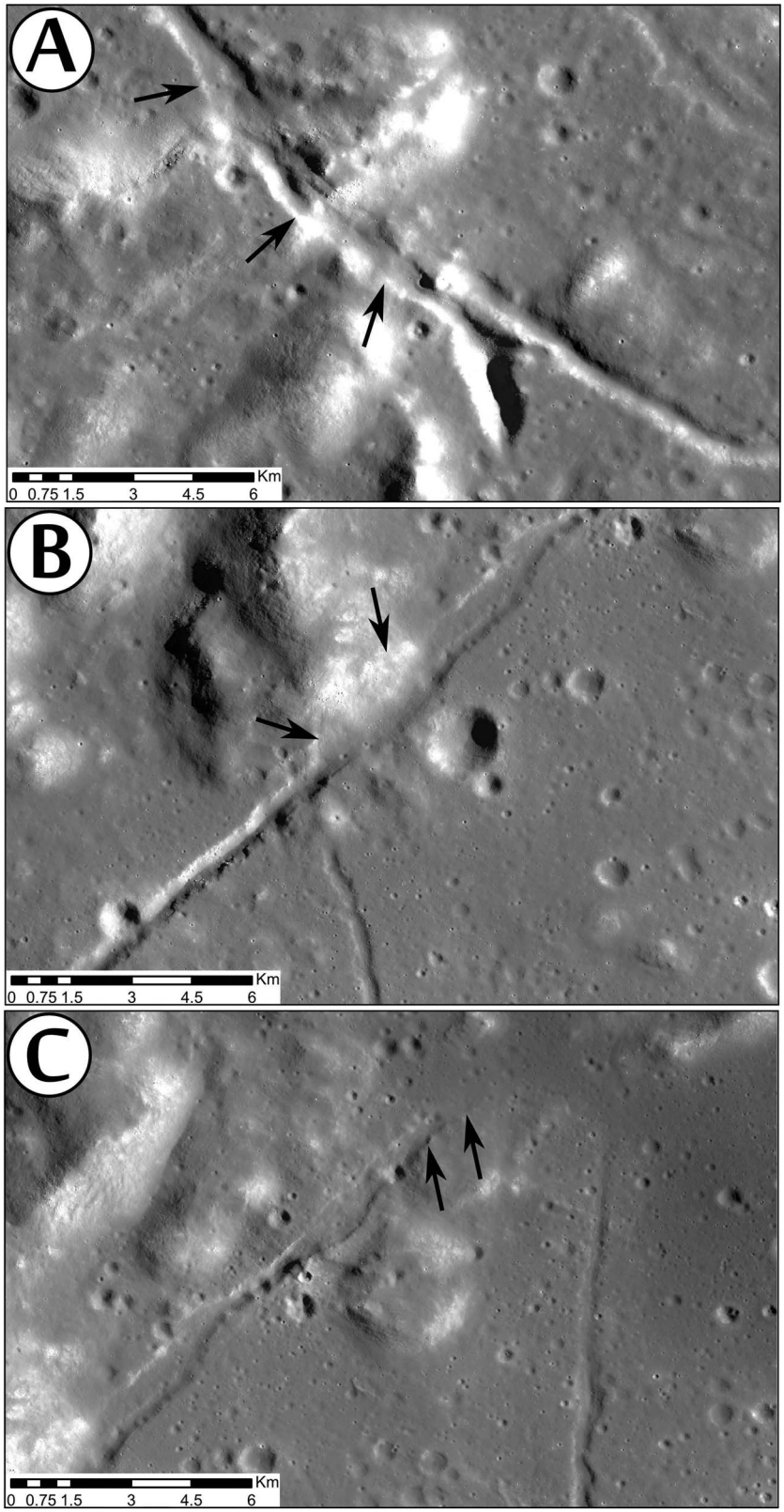

Figure 6. Zoomed Kaguya TC views from Figure 3b. The fractures are pointed at with arrows. (a) Central peak complex cross cut by a fracture. (b) Central alignment cut through by a fracture. (c) Volcanic deposit covering a fracture.

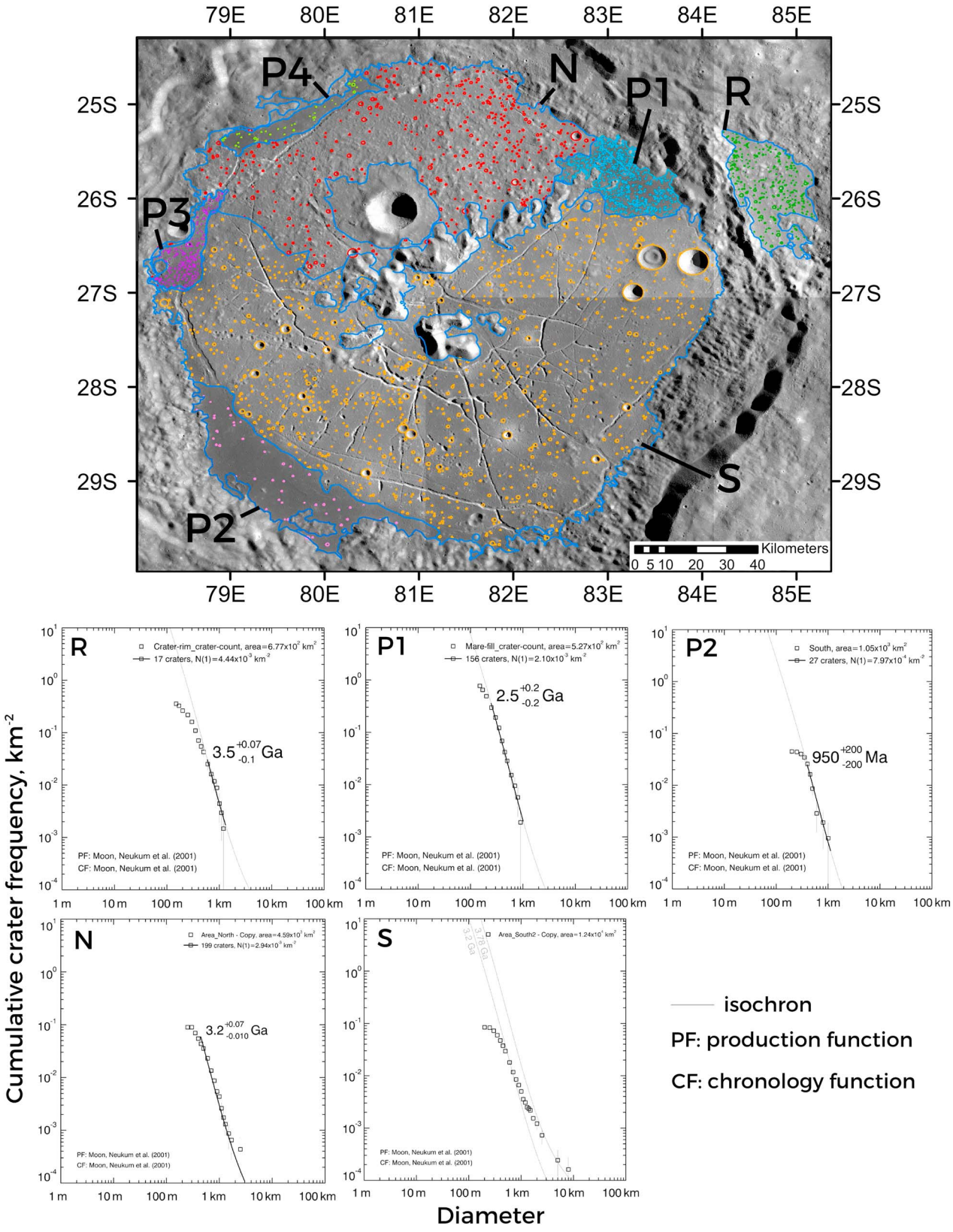

Figure 7. Humboldt crater count areas and locations displayed on a Kaguya TC mosaic. The northern part of Humboldt crater is labeled N, its southern part is labeled S, the volcanic deposits are labeled P_n, and the melt deposited on the Humboldt crater rim is labeled R. The topography and morphology helped delimiting the crater floor units.

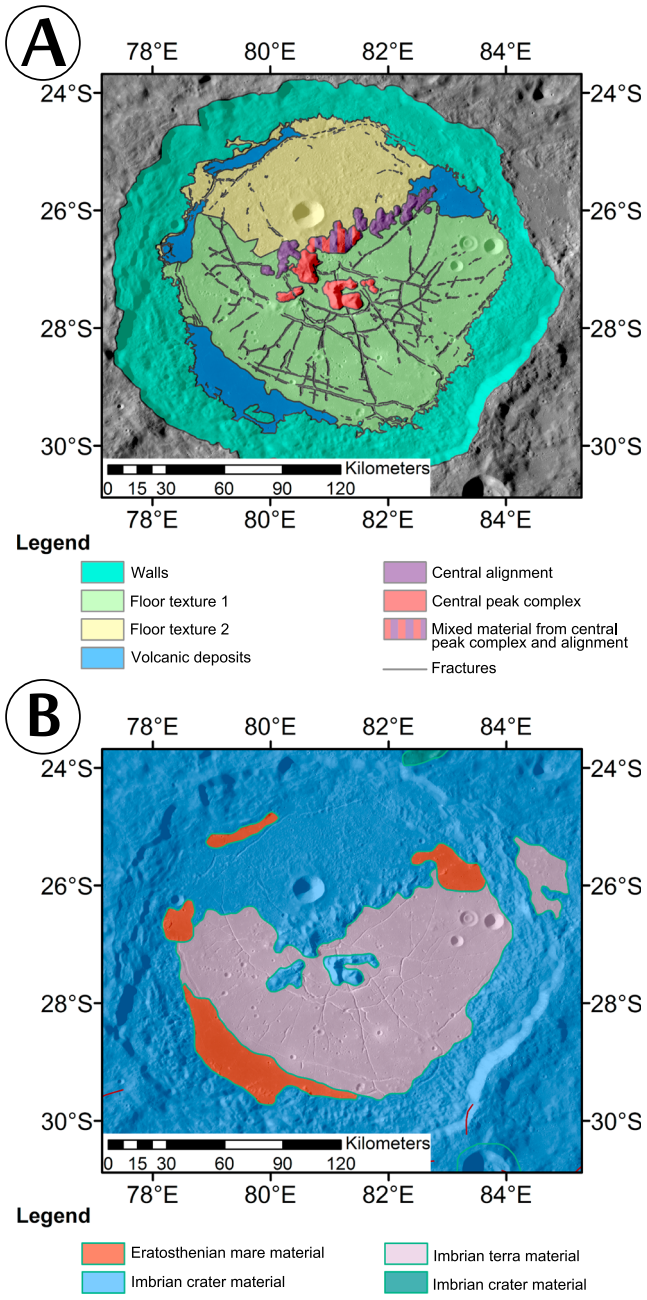

Figure 8. (a) Humboldt crater geologic map (this study) overlain on the LRO WAC mosaic. The part that is striped pink and purple is material likely pertaining both to the central peak complex and the central alignment. (b) Humboldt crater geologic map from Wilhelms and El-Baz (1977) overlain on the LRO WAC mosaic.

diameter superior to 250 m were used for age determination. The crater distributions of the volcanic deposits labeled P2, P3, and P4 are consistent within error with an age of 1 Ga. The crater counts performed on the volcanic deposit labeled P1 yield an older age of 2.5 Ga. The crater counts performed on the melt pool deposited on the rim of Humboldt crater result in an age of 3.5 Ga, which is consistent with the Humboldt crater age proposed by Wilhelms and El-Baz (1977).

The crater counts performed on the north floor unit and south floor units are more complex. Their respective crater distributions are irregular and exhibit plateaus that indicate resurfacing events. The fitted age of the north unit is probably a resurfacing event dated at 3.2 Ga, which is supported by its rugged texture (e.g., other craters' ejecta emplacement on the Humboldt crater floor, crater floor collapse). The same model age is plotted in the crater distribution of the south unit, but it does not fit the crater distribution. The floor fractures emplacement probably disturbed the surface, explaining part of the age fitting problem.

5. Discussion

5.1. Humboldt Crater's Geological Map

An updated geological map, based on high-resolution imagery and our mineralogical detections, is provided in Figure 8a. For comparison, the initial geological map of the crater by Wilhelms and El-Baz (1977), which combined crater floor, walls, and ejecta in one unit, is shown in Figure 8b. Shapefiles of the mapped units and floor fractures are provided in the supporting information. The volcanic deposits were mapped at higher resolution and expanded. The division between crater material and terra material (Floor texture 1 and 2, respectively, in the new map) is different as well. In this study, floor textures were used to distinguish between the two floor units on high-resolution imagery, which might explain the differences between the two geological maps.

5.2. Central Peak Complex and Central Alignment

The central peak complex and central alignment were mapped as distinct units when possible, using a combination of morphological, topographic, and mineralogical information. The altitude of the central peak complex is greater than the central alignment (Figure 1a). The central alignment exhibits a pyroxene signature, featureless spectra, and spectra displaying absorption features of both pyroxene and plagioclase interpreted as plagioclase-pyroxene mixture spectra. The unit mapped as mixed material (dashed unit in Figure 8a) is located between the central peak complex and the central alignment. It is difficult to distinguish it from the central peak complex unit or the central alignment unit, because it displays plagioclase spectra toward the central peak complex (southern part of the unit), and featureless spectra toward the crater floor (northern part of the unit).

Donaldson Hanna et al. (2014) described numerous pure crystalline plagioclase occurrences (<1% olivine and pyroxene in the rock) on the Humboldt crater central peak complex, which is in good agreement with our detections (Figure 3a). Featureless spectra are also detected on the Humboldt crater central peak complex. They exhibit no absorption feature at 1,000 and 2,000 nm and have been interpreted to be the signature of shocked plagioclase (Adams et al., 1979), or anorthosite affected by space weathering (Lucey, 2002). The multiple detections of pure crystalline plagioclase throughout the Humboldt crater central peak complex hint at the crustal origin of the material composing it.

Song et al. (2013) calculated the proximity value of the Humboldt crater central peak complex. Cahill et al. (2009) defined the proximity value to the crust-mantle interface as the difference between the crustal

thickness and the minimum depth of origin of the crater's central peak complex (which is equal to the maximum depth of melting, Cintala and Grieve, 1998). Song et al. (2013) calculated that the Humboldt crater central peak complex material originates from the lower crust, about 2 km above the crust-mantle interface. This result was corroborated by Martinot et al. (2017), who calculated the Humboldt crater proximity value to the crust-mantle interface with the GRAIL crustal thickness models (Wieczorek et al., 2013), using Flahaut et al. (2012) method for estimating the preimpact crustal thickness of Humboldt crater. Martinot et al. (2017) found that the Humboldt crater-forming event likely tapped material previously residing down to within <10 km of the crust-mantle interface. Song et al. (2013) calculated the CF value of the Humboldt crater central peak complex and found it more consistent with an anorthositic composition than a mafic composition. This corroborates the crustal origin of the material composing the Humboldt crater central peak complex and challenges the LMO crystallization view that a more mafic lithology should be encountered closer to the crust-mantle interface (e.g., Lin et al., 2017; Snyder et al., 1992). Ohtake et al. (2009) defined a purest anorthosite (PAN) rock composed of nearly 100% anorthosite. Ohtake et al. (2009) and Donaldson Hanna et al. (2014) proposed the existence of a PAN-rich global layer in the crust. This PAN-rich layer might be sampled by Humboldt crater central peak complex. Alternatively, the crust-mantle interface might be found at greater depth than expected.

Despite its spectral and spatial predominance, plagioclase is not the only mineral detected on the Humboldt crater central peak complex. Olivine, glass, and plagioclase-pyroxene mixture spectra are marginally observed on one of the mounds of the western part of the central peak complex. Lemelin et al. (2015) suggested the presence of heterogeneities in the crust, which is consistent with Pieters et al. (2011) and Jozwiak, Head, Neumann, and Wilson (2016) conclusions. The presence of these mafic lithologies could hint at the presence of a crustal heterogeneity sampled by the Humboldt crater central peak complex. Two olivine occurrences and three glass detections are located close to a floor fracture. These minerals may be secondary: they may have crystallized from a volcanic event or recrystallized from the impact melt. There are signs of volcanism on the Humboldt crater floor (pyroclastic deposits and vents associated to floor fractures, Jozwiak, Head, & Wilson, 2016). However, no visible sign of a volcanic vent close to the central peak complex has been observed, and there is no obvious sign of impact melt on the Humboldt crater central peak complex. Alternatively, the glass could have an impact origin. Tompkins and Pieters (2010) indicated that spectrally distinguishing a volcanic glass from an impact glass is difficult. The olivine could be endogenic, being presumably abundant in the lunar mantle and lower crust (e.g., Elardo et al., 2011; Lin et al., 2017; Snyder et al., 1992). The fact that the olivine and glass occurrences are spatially limited to a small mound peripheral to the central peak complex leads us to prefer the hypothesis of a secondary origin for these detections (e.g., melt recrystallization).

5.3. Crater Floor and Volcanic Deposits

Four HCP-rich, volcanic deposits are emplaced in topographic lows in the periphery of the Humboldt crater floor (Gaddis et al., 2003, Figure 1a). Jozwiak et al. (2012) showed that floor-fractured craters are formed by the intrusion of a magmatic body beneath the crater. Subsequently, Jozwiak, Head, Neumann, and Wilson (2016) observed the band-filtered Bouguer solution of Humboldt crater in order to be able to determine density anomalies in the crust. They found that the Humboldt crater volcanic deposits are spatially correlated with positive crustal density anomalies. Thorey et al. (2015) showed that positive signatures in a floor-fractured crater gravity field are consistent with the presence of shallow magmatic intrusions beneath its surface. Such magmatic intrusions could extrude volatile-rich pockets toward the crater floor. The wide age range of the Humboldt crater volcanic deposits could be explained by volatile heterogeneities in the magmatic intrusions, generating different volatile-rich pockets that reach the surface staggered in time.

Crater counts were performed on the volcanic deposits (P1 through P4, locations indicated in Figure 7). The crater distributions on the Humboldt crater volcanic deposits are often irregular, which could lead to an incorrect absolute age. However, the relative age is reliable, and the significant age difference between P1, on the one hand, and P2–P4, on the other hand, leads us to think that Humboldt crater had several episodes of volcanic activity, spanning a period exceeding 1 Ga. Signs of long lasting volcanic activity (spanning about 2.7 Ga) were found by Hiesinger (2003) while performing crater counts on mare basalts on the near side. They also found young mare basalts (1.2 Ga old), similar to the model age of the Humboldt crater volcanic deposits P2 through P4. Humboldt crater volcanic deposits have been described as pyroclastic deposits by Gaddis et al. (2003). Caution needs to be taken when counting craters on pyroclastics, since they can be deposited in very thin layers (Gaddis et al., 2003). A cratered surface covered by a thin layer of pyroclastics might retain its topography, challenging crater count dating. The absolute ages obtained need to be considered with caution.

The crater counts performed on the north and the south units have a common model age at 3.2 Ga. In the northern crater floor unit, this model age fits the distribution of the craters between 300 m and 1 km in diameter. In the southern crater floor unit, it fits the distribution of the craters between 300 m and 750 m. The 3.2 Ga isochron does not fit bigger craters, which suggests that the crater floor is older. No isochron fits the south unit distribution of craters between 750 m and 8 km in diameter. This suggests that the unit was resurfaced. This resurfacing process may have decreased in intensity from 3.2 Ga onward, which might explain the model age observed.

Yamamoto et al. (2010) detected olivine in the walls of a small crater on the Humboldt crater floor using SP data. SP is a continuous line spectrometer with a swath of 500 m, and a spatial resolution of 500 m per pixel (Matsunaga et al., 2008). Due to the nature of operations and lifetime of the mission and instrument, SP did not cover the whole lunar surface, contrary to M^3. This explains the more numerous olivine occurrences detected here. The olivine occurrence in the walls of the small crater on the Humboldt crater floor is associated with glass. These olivines probably crystallized from the melt generated during the small impact crater-forming event.

Several occurrences of a pyroxene-plagioclase mixture were detected in the southwest of the crater, in association with fresh impact craters. The floor of Humboldt crater does not display a strong spectral signature, except near impact craters, which expose underlying, fresher material. This means that the mineralogy beneath the Humboldt crater floor is plagioclase and pyroxene rich, at least in the southwest of the crater.

Jozwiak, Head, Neumann, and Wilson (2016) recently showed that the Humboldt crater floor displays a positive Bouguer anomaly slightly offset from the crater center. The floor fractures observed in Humboldt crater were mapped by Jozwiak, Head, and Wilson (2016) (Figure 1a) and differentiated into several categories. Two categories are represented in Figure 6. The fractures in Figures 6a and 6b were classified as "v" fractures, forming during the uplift of the crater floor associated with the magmatic intrusion emplacement and resulting in the brittle fracturing of the crater floor (Jozwiak, Head, & Wilson, 2016). The fracture in Figure 6c was classified as a graben. The fractures are cross-cutting parts of the central peak complex (Figure 6a), as well as the central alignment (Figure 6b). This means that the central peak complex and central alignment predate the fractures. Volcanic deposits are overlying the fractures (Figure 6c), which constrains the formation of the volcanic deposits to be younger than the fractures. This corroborates the crater counting results.

The south facing sides of the central alignment are smooth (Figure 3b) and similarly oriented, comparable to the morphology of a fault wall. No reference layer was found, making it harder to determine the fault movement. A fault cutting the northeast rim of Humboldt crater (Figure 1b) is observed. Segments of this fault are observed over more than 100 km. The presence of a preexisting fault could explain the slight altitude difference between the northern and southern floor units (80 m), accommodating part of the stress caused by the intrusion of a magmatic body beneath the Humboldt crater floor.

The rugged morphology and altitude of the northern floor unit could be explained by the destabilization of the crater walls leading to the emplacement of debris on the crater floor. This resurfacing event could explain the observed crater distribution of the northern floor unit at 3.2 Ga (Figure 7). The presence of debris on the crater floor could also explain why fewer floor fractures are observed on the northern floor unit than on the southern floor unit. The existence of a discontinuity (e.g., fault) before the formation of Humboldt crater could be reflected in its final morphology and lead to the formation of the multiple peaks forming the central alignment. The central alignment could alternatively have been triggered by local or regional stresses after Humboldt crater formation.

5.4. Crater Walls and Rim

The rim of Humboldt crater is asymmetric, with the altitude of its northern rim being lower than that of its southern rim (Figure 1c). A lobe of ejecta from Humboldt crater is deposited on top of the Hecataeus crater floor, to the north of Humboldt crater (Figure 1a), constraining Humboldt crater to be younger than Hecataeus crater. The formation of Humboldt crater on an irregular preimpact surface can explain the unevenness of its rim (Figure 1a). The melt sheet is observed to the northeast of the Humboldt crater rim (Hawke & Head, 1977) (labeled R in Figure 7). Crater counts of this melt sheet constrain the minimum age of the Humboldt crater formation to 3.5 Ga, which is consistent with the upper Imbrian age of the Humboldt crater material proposed by Wilhelms and El-Baz (1977).

Several glass detections are located in the Humboldt crater walls and rims (Figure 3a). Impact melt distribution has been studied on terrestrial impact craters (Osinski, 2004), showing that impact melt can be deposited on the walls of a crater. This could confirm an impact origin of the glass detections of the walls of Humboldt crater, by recrystallization of the melt produced during the Humboldt crater-forming event. The glass detections observed in the walls and rims of Humboldt crater are associated with small impact craters (<1 km in diameter) that expose underlying material. The glass could have crystallized from the Humboldt crater-forming event and be later exposed by subsequent small impact craters.

Some olivine occurrences are found in the terraced walls and rims of the Humboldt crater (Figure 3a) and located near fresh impact craters. Small impact crater-forming events rework the target material and lead to the exposure of fresh material. If the olivine occurrences are distributed evenly through the crater's walls and ejecta, then they might originate from the target material (i.e., below the surface). However, if the olivine exposures are only concentrated around the small crater, then they may be secondary and have recrystallized from impact melt. Here the olivines are located close to the small craters and not spread out in the small crater ejecta, hinting at a secondary origin (e.g., melt recrystallization). Alternatively, these olivines could be exogenic: olivine is abundant in asteroids, meteorites, and chondrules (e.g., Brearley & Jones, 1998; Mittlefehldt et al., 1998).

The observation of spinel and olivine in the east walls, and olivine and glass in the south walls of Humboldt crater is interesting because they are observed in the same crater unit. This raises the question of the origin of these minerals, which cannot be accounted for by existing petrogenetic models. The spinel occurrences are typically a few hundred meters across. Spinel detections on the Moon were located within craters and volcanic domes on the nearside (Dhingra et al., 2011) and the farside (Kaur et al., 2013; Pieters et al., 2011, 2014). Pieters et al. (2011) indicated that the detection of spinel constrains the abundance of other mafic minerals (olivine and pyroxene) to less than 5% and defined a rock composed of "pink" spinel (owing to the color of Mg-spinels found in lunar samples) and anorthite (PSA).

Several explanations are possible for the spinel detections. It could have an endogenic or an exogenic origin. Pieters et al. (2011) proposed that the origin of olivine and Mg-rich spinel could be linked with plutonic events, resulting in the intrusion of magmatic bodies into the lower crust. The composition of the olivine occurrences (forsteritic) is consistent with a deep origin. Prissel et al. (2014) listed two endogenic petrogenetic models for PSA formations: magma-wall rock interactions in the lunar crust (Gross et al., 2011), and crystallization of a melt mixture between the anorthositic crust and mantle material (Vaughan et al., 2013). Lin et al. (2017) performed crystallization experiments to simulate lunar magma ocean solidification in water-bearing conditions. The results of their experiments show that spinel is among the last minerals to be crystallized during solidification of a water-bearing magma ocean. They calculated that a spinel-bearing layer could be found around 30 km underneath the surface after magma ocean solidification. The walls of Humboldt crater are not likely to cut through 30 km of crust (estimated thickness from GRAIL model 1, Wieczorek et al., 2013). However, we note that the 880 km pre-Nectarian Australe basin is located 300 km to the south-southeast of Humboldt crater (Wilhelms & El-Baz, 1977). Australe basin likely ejected deep crustal to mantle material in its ejecta blanket during its formation, which might have been sampled by the Humboldt impact crater-forming event. Most of the spinel detections are concentrated on the southeast walls of Humboldt crater, close to Barnard crater. The south-eastern rims of Humboldt crater are intact, which hints that Humboldt crater was formed after Barnard crater. This could imply that Barnard crater reworked the Australe basin ejecta during its formation, later redisturbed by the Humboldt crater-forming event, leading to the observed dichotomy in the spinel exposures of the south-eastern walls of Humboldt crater.

5.5. Implications for the Lunar Crustal Structure

This study showed that understanding the geological setting of a crater is important in order to interpret the crustal structure of its region. The mineralogical signature of the Humboldt crater central peak complex, floor, and walls hint that the Humboldt crater-forming event took place in a complex setting. The anorthosite signature of the Humboldt crater central peak complex reflects a crustal signature. However, the olivine and spinel detections observed in the Humboldt crater walls suggest the presence of preimpact heterogeneities in the crust. These heterogeneities could have been generated by the emplacement of a pluton in the crust sampled by the Humboldt crater-forming event. The observation of a Mg-rock type composed of less than

5% mafic minerals in craters of the lunar farside by Pieters et al. (2011) supports this hypothesis. Alternatively, the presence of Australe basin ejecta in the crust before the formation of the Humboldt crater might explain the observed mineralogy.

6. Conclusion

A custom-made continuum removal routine for M^3 data allowed the mineralogical characterization of the Humboldt crater central peak complex, floor, central alignment, walls, and rim. The mineralogy of Humboldt crater reflects its complex geology. The Humboldt crater central peak complex is anorthosite-rich — hinting at a crustal origin — whereas multiple mafic minerals (spinel, pyroxene, and olivine) and glass occurrences are detected in the walls and rim of the crater.

The Humboldt crater-forming event most likely took place on a disturbed surface, marked by the presence of Hecataeus crater to the north, Phillips crater to the west, and Barnard crater to the southeast. The surface was probably covered by the ejecta of Australe basin, reworked by Barnard crater, which can explain the presence of olivine, glass, and spinel in the walls of Humboldt crater. Alternatively, the Humboldt crater-forming event might have sampled a mafic pluton in the crust.

The orientation of the central alignment observed in Humboldt crater is the same as that of a fault located to the northeast of Humboldt crater. This, and the smooth south facing slopes of the central alignment, hints that it is a tectonic discontinuity that existed before Humboldt crater was formed.

Crater counts were performed on different units of Humboldt crater. The age results are consistent with the observed stratigraphic relationships between the units. The age obtained from the crater counts performed on the crater volcanic deposits span a period of over a billion years, suggesting a long duration of a volcanic activity within the Humboldt crater. This could be explained by the presence of volatile distribution heterogeneities in a magmatic intrusion underneath the crater, extruding volatile-rich pockets staggered in time.

The study of the lunar structure through impact craters is possible, but caution needs to be used in order to identify the origin of the mineralogical detections. The minerals can have a secondary origin: they may have recrystallized from the impact melt or be part of the ejecta of an older impact structure. The minerals may otherwise have a primary origin and reflect the crystallization of the lunar magma ocean. Primary minerals give important insight on the stratification of the crust, and on the presence of crustal heterogeneities.

Acknowledgments
We are grateful to J. L. Whitten and an unknown reviewer for their insightful remarks and suggestions. We thank the e-Mars team in Lyon (http://e-mars.geologie-lyon.fr/), Y. Lin, K. Donaldson-Hanna, M. Ohtake, S. Yamamoto, D. Dhingra, B. Horgan, L. Cheek, R. Klima, D. Kring, and G. Osinski for kindly sharing their data and for fruitful discussions. This work was supported by a Netherlands Organization for Scientific Research (NWO). Vici grant and a User Support Space Research grant from the Netherlands Space Office (NSO) to W. v. W. C. Q. N. is supported by European Research Council through the FP7/2007-2013/ERC grant agreement 280168. M^3 and LRO data can be accessed in the PDS Geoscience Node, Lunar Orbital Data Explorer (http://ode.rsl.wustl.edu/). SELENE data can be accessed on the SELENE data archive (http://l2db.selene.darts.isas.jaxa.jp/index.html.en). The LRO LOLA and Kaguya Terrain Camera DEM merge can be accessed on the USGS Astrogeology Science Center (https://astrogeology.usgs.gov/search/map/Moon/LRO/LOLA/Lunar_LRO_LrocKaguya_DEMmerge_60N60S_512ppd). The data used in this study are attached as supporting information and are also available upon request from the main author (m.martinot@vu.nl).

References

Adams, J., Hörz, F., & Gibbons, R. (1979). Effects of shock-loading on the reflectance spectra of plagioclase, pyroxene, and glass. In *Inproceedings of the 10th Lunar and Planetary Science Conference* (pp. 5–7).

Adams, J. B. (1974). Visible and near-infrared diffuse reflectance spectra of pyroxenes as applied to remote sensing of solid objects in the solar system. *Journal of Geophysical Research*, *79*(32), 4829–4836. https://doi.org/10.1029/JB079i032p04829

Adams, J. B., & Goullaud, L. H. (1978). Plagioclase feldspars: Visible and near infrared diffuse reflectance spectra as applied to remote sensing. In *Lunar and Planetary Science Conference Proceedings* (Vol. 9, pp. 2901–2909).

Adams, J. B., Pieters, C., & McCord, T. B. (1974). Orange glass: Evidence for regional deposits of pyroclastic origin on the moon. *Lunar Science Conference*, *1*, 171–186.

Baker, D. M. H., Head, J. W., Fassett, C. I., Kadish, S. J., Smith, D. E., Zuber, M. T., & Neumann, G. A. (2011). The transition from complex crater to peak-ring basin on the Moon: New observations from the Lunar Orbiter Laser Altimeter (LOLA) instrument. *Icarus*, *214*(2), 377–393. https://doi.org/10.1016/j.icarus.2011.05.030

Baldwin, R. B. (1968). Rille pattern in the Lunar Crater Humboldt. *Journal of Geophysical Research*, *73*(10), 3227–3229.

Barker, M. K., Mazarico, E., Neumann, G. A., Zuber, M. T., Haruyama, J., & Smith, D. E. (2016). A new lunar digital elevation model from the Lunar Orbiter Laser Altimeter and SELENE Terrain Camera. *Icarus*, *273*, 346–355. https://doi.org/10.1016/j.icarus.2015.07.039

Beer, W., & Madler, J. H. (1837). *Der Mond Nach Seinen Komischen Und Individuellen Verhaltnissen Oder Allgemeine Vergleichende Selenographie: Mit Besondrer Beziehung Auf Die Verfassern Herausgegebene Mapppa Selenographica* (schopp ed., pp. 1–425). Berlin.

Besse, S., Sunshine, J. M., & Gaddis, L. R. (2014). Volcanic glass signatures in spectroscopic survey of newly proposed lunar pyroclastic deposits. *Journal of Geophysical Research: Planets*, *119*, 1–21. https://doi.org/10.1002/2013JE004518

Besse, S., Sunshine, J. M., Staid, M. I., Boardman, J., Pieters, C., Guasqui, P., … Li, J. Y. (2013). A visible and near-infrared photometric correction for Moon Mineralogy Mapper (M^3). *Icarus*, *222*, 229–242. https://doi.org/10.1016/j.icarus.2012.10.036

Boardman, J. W., Pieters, C. M., Green, R. O., Lundeen, S. R., Varanasi, P., Nettles, J., … Taylor, L. A. (2011). Measuring moonlight: An overview of the spatial properties, lunar coverage, selenolocation, and related Level 1B products of the Moon Mineralogy Mapper. *Journal of Geophysical Research*, *116*, E00G14. https://doi.org/10.1029/2010JE003730

Brearley, A. J., & Jones, R. H. (1998). Chondritic meteorites. *Reviews in Mineralogy and Geochemistry*, 36(1), 3–1.

Burns, R. G. (1993). *Mineralogical applications of crystal field theory* (Vol. 5). Cambridge University Press.

Burns, R. G. (1970). Crystal field spectra and evidence of cation ordering in olivine minerals. *American Mineralogist*, *55*, 1608–1632.

Cahill, J. T. S., Lucey, P. G., & Wieczorek, M. A. (2009). Compositional variations of the lunar crust: Results from radiative transfer modeling of central peak spectra. *Journal of Geophysical Research*, *114*, E09001. https://doi.org/10.1029/2008JE003282

Cheek, L. C., Donaldson Hanna, K. L., Pieters, C. M., Head, J. W., & Whitten, J. L. (2013). The distribution and purity of anorthosite across the Orientale basin: New perspectives from Moon Mineralogy Mapper data. *Journal of Geophysical Research: Planets*, *118*, 1805–1820. https://doi.org/10.1002/jgre.20126

Cheek, L. C., & Pieters, C. M. (2014). Reflectance spectroscopy of plagioclase-dominated mineral mixtures: Implications for characterizing lunar anorthosites remotely. *American Mineralogist*, *99*(10), 1871–1892. https://doi.org/10.2138/am-2014-4785

Cheek., L. C., Pieters, C. M., Dyar, M. D. K, & Milam, A. (2009). Revisiting plagioclase optical properties for lunar exploration. In *40th Lunar and Planetary Science Conference, (Lunar and Planetary Science XL), held March 23–27, 2009* (id.1928). The Woodlands, TX.

Cintala, M. J., & Grieve, R. A. F. (1998). Scaling impact melting and crater dimensions: Implications for the lunar cratering record. *Meteoritics & Planetary Science*, *33*(4), 889–912. https://doi.org/10.1111/j.1945-5100.1998.tb01695.x

Clark, R. N., Pieters, C. M., Green, R. O., Boardman, J. W., & Petro, E. N. (2011). Thermal removal from near-infrared imaging spectroscopy data of the Moon. *Journal of Geophysical Research*, *116*, E00G16. https://doi.org/10.1029/2010JE003751

Cloutis, E. A., Sunshine, J. M., & Morris, R. V. (2004). Spectral reflectance-compositional properties of spinels and chromites: Implications for planetary remote sensing and geothermometry. *Meteoritics & Planetary Science*, *39*(4), 545–565. https://doi.org/10.1111/j.1945-5100.2004.tb00918.x

Dhingra, D., Pieters, C. M., Boardman, J. W., Head, J. W., Isaacson, P. J., & Taylor, L. A (2011). Compositional diversity at Theophilus Crater: Understanding the geological context of Mg-spinel bearing central peaks. *Geophysical Research Letters*, *38*, L11201. https://doi.org/10.1029/2011GL047314

Donaldson Hanna, K. L., Cheek, L. C., Pieters, C. M., Mustard, J. F., Greenhagen, B. T., Thomas, I. R., & Bowles, N. E. (2014). Global assessment of pure crystalline plagioclase across the Moon and implications for the evolution of the primary crust. *Journal of Geophysical Research: Planets*, *119*, 1516–1545. https://doi.org/10.1002/2013JE004476

Elardo, S. M., Draper, D. S., & Shearer, C. K. (2011). Lunar Magma Ocean crystallization revisited: Bulk composition, early cumulate mineralogy, and the source regions of the highlands Mg-suite. *Geochimica et Cosmochimica Acta*, *75*(11), 3024–3045. https://doi.org/10.1016/j.gca.2011.02.033

Flahaut, J., Blanchette-Guertin, J.-F., Jilly, C., Sharma, P., Souchon, A., Van Westrenen, W., & Kring, D. A. (2012). Identification and characterization of science-rich landing sites for lunar lander missions using integrated remote sensing observations. *Advances in Space Research*, *50*(12), 1647–1665. https://doi.org/10.1016/j.asr.2012.05.020

Gaddis, L. R., Staid, M. I., Tyburczy, J. A., Hawke, B. R., & Petro, N. E. (2003). Compositional analyses of lunar pyroclastic deposits. *Icarus*, *161*(2), 262–280. https://doi.org/10.1016/S0019-1035(02) 00036-2

Green, R. O., Pieters, C., Mouroulis, P., Eastwood, M., Boardman, J., Glavich, T., … Wilson, D. (2011). The Moon Mineralogy Mapper (M^3) imaging spectrometer for lunar science: Instrument description, calibration, on-orbit measurements, science data calibration and on-orbit validation. *Journal of Geophysical Research*, *116*, E00G19. https://doi.org/10.1029/2011JE003797

Gross, J., Treiman, A. H., & Le, L. (2011). Unique spinel-rich lithology in lunar meteorite ALHA81005: Origin and possible connection to M^3 observations of the farside highlands. *Lunar and Planetary Science Conference*, *42*, 2–3.

Haruyama, J., Matsunaga, T., Ohtake, M., Morota, T., Honda, C., Yokota, Y., … Ogawa, Y. (2008). Global lunar-surface mapping experiment using the Lunar imager/spectrometer on SELENE. *Earth, Planets and Space*, *60*(4), 243–255.

Hawke, B. R., & Head, J. W. (1977). Impact melt on lunar crater rims. In *Impact and Explosion Cratering: Planetary and Terrestrial Implications; Proceedings of the Symposium on Planetary Cratering Mechanics* (pp. 815–841). Flagstaff, AZ, New York: Pergamon Press, Inc. https://doi.org/10.1017/CBO9781107X00000

Head, J. W., & Wilson, L. (1992a). Lunar mare volcanism: Stratigraphy, eruption conditions, and the evolution of secondary crusts. *Geochimica et Cosmochimica Acta*, *56*(6), 2155–2175. https://doi.org/10.1016/0016-7037(92)90183-J

Head, J. W. I., & Wilson, L. (1992b). Lunar mare volcanism - Stratigraphy, eruption conditions, and the evolution of secondary crusts. *Geochimica et Cosmochimica Acta*, *56*, 2155–2175. https://doi.org/10.1016/0016-7037(92) 90183-J

Hiesinger, H. (2003). Ages and stratigraphy of mare basalts in Oceanus Procellarum, Mare Nubium, Mare Cognitum, and Mare Insularum. *Journal of Geophysical Research*, *108*(E7), 5065. https://doi.org/10.1029/2002JE001985

Horgan, B. H. N., Cloutis, E. A., Mann, P., & Bell, J. F. (2014). Near-infrared spectra of ferrous mineral mixtures and methods for their identification in planetary surface spectra. *Icarus*, *234*, 132–154. https://doi.org/10.1016/j.icarus.2014.02.031

Jozwiak, L. M., Head, J. W. I., Neumann, G. A., & Wilson, L. (2016). Observational constraints on the identification of shallow lunar magmatism: Insights from floor-fractured craters. *Icarus*, *0*, 1–8. https://doi.org/10.1016/j.icarus.2016.04.020

Jozwiak, L. M., Head, J. W., & Wilson, L. (2016). An analysis of eruption styles in lunar floor-fractured craters. In *Lunar and Planetary Science Conference* (Vol. 47, 1169 pp.).

Jozwiak, L. M., Head, J. W., Zuber, M. T., Smith, D. E., & Neumann, G. A. (2012). Lunar floor-fractured craters: Classification, distribution, origin and implications for magmatism and shallow crustal structure. *Journal of Geophysical Research*, *117*, E11005. https://doi.org/10.1029/2012JE004134

Kaula, W. M. (1979). Thermal evolution of Earth and Moon growing by planetesimal impacts. *Journal of Geophysical Research*, *84*(2), 999–1008. https://doi.org/10.1029/JB084iB03p00999

Kaur, P., Chauhan, P., & Ajai, S. A. C. (2013). Exposures of Mg-spinel on an evolved silicic lithology Hansteen Alpha on the Moon. In *44th Lunar and Planetary Science Conference, held March 18–22, 2013* (1348 pp.). The Woodlands, TX: LPI Contribution No. 1719.

Klima, R. L., Pieters, C. M., & Dyar, M. D. (2007). Spectroscopy of synthetic Mg-Fe pyroxenes I: Spin-allowed and spin-forbidden crystal field bands in the visible and near-infrared. *Meteoritics & Planetary Science*, *42*(2), 235–253. https://doi.org/10.1111/j.1945-5100.2007.tb00230.x

Lemelin, M., Lucey, P. G., Song, E., & Taylor, G. J. (2015). Lunar central peak mineralogy and iron content using the Kaguya Multiband Imager: Reassessment of the compositional structure of the lunar crust. *Journal of Geophysical Research: Planets*, *120*, 869–887. https://doi.org/10.1002/2014JE004778

Lin, Y., Tronche, E. J., Steenstra, E. S., & van Westrenen, W. (2017). Evidence for an early wet Moon from experimental crystallization of the lunar magma ocean. *Nature Geoscience*, *10*(1), 14–18. https://doi.org/10.1038/ngeo2845

Logan, L. M., Hunt, G. R., Salisbury, J. W., & Balsamo, S. R. (1973). Compositional implication of Christiansen frequency maximums for infrared remote sensing applications. *Journal of Geophysical Research*, *78*(23), 430–450. https://doi.org/10.1029/JB078i023p04983

Lucey, P. G. (2002). Radiative transfer model constraints on the shock state of remotely sensed lunar anorthosites. *Geophysical Research Letters*, *29*(10), 1486. https://doi.org/10.1029/2001GL014655

Martinot, M., Flahaut, J., Besse, S., Quantin, C., Van Westrenen, W., Donaldson Hanna, K. L., & Blanchette-Guertin, J.-F. (2017). Lunar crustal composition in the Humboldt crater region. In *Lunar and Planetary Science Conference* (Vol. 48).

Matsunaga, T., Ohtake, M., Haruyama, J., Ogawa, Y., Nakamura, R., Yokota, Y., … Otake, H. (2008). Discoveries on the lithology of lunar crater central peaks by SELENE spectral profiler. *Geophysical Research Letters*, *35*, L23201. https://doi.org/10.1029/2008GL035868

Melosh, H. J. (1989). Impact cratering: A geologic process. In *Research supported by NASA. New York, Oxford University Press (Oxford Monographs on Geology and Geophysics, No. 11)* (253 pp.).
Michael, G. G., & Neukum, G. (2010). Planetary surface dating from crater size-frequency distribution measurements: Partial resurfacing events and statistical age uncertainty. *Earth and Planetary Science Letters*, *294*(3–4), 223–229. https://doi.org/10.1016/j.epsl.2009.12.041
Mittlefehldt, D. W., McCoy, T. J., Goodrich, C. A., & Kracher, A. (1998). Non-chondritic meteorites from asteroidal bodies. *Reviews in Mineralogy and Geochemistry*, 36(1), 4–1.
Mustard, J. F., Pieters, C. M., Isaacson, P. J., Head, J. W., Besse, S., Clark, R. N., … Tompkins, S. (2011). Compositional diversity and geologic insights of the Aristarchus crater from Moon Mineralogy Mapper data. *Journal of Geophysical Research*, *116*, E00G12. https://doi.org/10.1029/2010JE003726
Neukum, G. (1983). *Meteorite bombardment and dating of planetary surfaces (Meteoritenbombardement und Datierung planetarer Oberflächen)*, (PhD thesis). University of Munich.
Neukum, G., Ivanov, B. A., & Hartmann, W. K. (2001). Cratering records in the inner solar system in relation to the lunar reference system. *Space Science Reviews*, *96*(1/4), 55–86.
Ohtake, M., Matsunaga, T., Haruyama, J., Yokota, Y., Morota, T., Honda, C., … Josset, J.-L. (2009). The global distribution of pure anorthosite on the Moon. *Nature*, *461*(7261), 236–240. https://doi.org/10.1038/nature08317
Osinski, G. R. (2004). Impact melt rocks from the Ries structure, Germany: An origin as impact melt flows? *Earth and Planetary Science Letters*, *226*(3–4), 529–543. https://doi.org/10.1016/j.epsl.2004.08.012
Pieters, C. M., Besse, S., Boardman, J., Buratti, B., Cheek, L., Clark, R. N., … Whitten, J. (2011). Mg-spinel lithology: A new rock type on the lunar farside. *Journal of Geophysical Research*, *116*, E00G08. https://doi.org/10.1029/2010JE003727
Pieters, C. M., Boardman, J., Buratti, B., Chatterjee, A., Clark, R., Glavich, T., … White, M. (2009). The Moon Mineralogy Mapper (M^3) on Chandrayaan-1. *Current Science*, *96*(4), 500–505.
Pieters, C. M., Donaldson Hanna, K., Cheek, L., Deepak, D., Prissel, T., Jackson, C., … Taylor, L. A. (2014). The distribution of Mg-spinel across the Moon and constraints on crustal origin. *American Mineralogist*, *99*, 1893–1910. https://doi.org/10.2138/am-2014-4776
Prissel, T. C., Parman, S. W., Jackson, C. R. M., Rutherford, M. J., Hess, P. C., Head, J. W., … Pieters, C. M. (2014). Pink Moon: The petrogenesis of pink spinel anorthosites and implications concerning Mg-suite magmatism. *Earth and Planetary Science Letters*, *403*, 144–156. https://doi.org/10.1016/j.epsl.2014.06.027
Robinson, M. S., Brylow, S. M., Tschimmel, M., Humm, D., Lawrence, S. J., Thomas, P. C., … Hiesinger, H. (2010). Lunar reconnaissance orbiter camera (LROC) instrument overview. *Space Science Reviews*, *150*(1–4), 81–124. https://doi.org/10.1007/s11214-010-9634-2
Schultz, P. H. (1976). Floor-fractured lunar craters. *The Moon*, *15*(3–4), 241–273. https://doi.org/10.1007/BF00562240
Shearer, C. K., Hess, P. C., Wieczorek, M. A., Pritchard, M. E., Parmentier, E. M., Borg, L. E., … Wiechert, U. (2006). Thermal and magmatic evolution of the Moon. *Reviews in Mineralogy and Geochemistry*, *60*(1610), 365–518. https://doi.org/10.2138/rmg.2006.60.4
Smith, D. E., Zuber, M. T., Neumann, G. A., Lemoine, F. G., Mazarico, E., Torrence, M. H., … Bartels, A. E. (2010). Initial observations from the Lunar Orbiter Laser Altimeter (LOLA). *Geophysical Research Letters*, *37*, L18204. https://doi.org/10.1029/2010GL043751
Snyder, G. A., Taylor, L. A., & Neal, C. R. (1992). A chemical model for generating the sources of mare basalts: Combined equilibrium and fractional crystallization of the lunar magmasphere. *Geochimica et Cosmochimica Acta*, *56*, 3809–3823.
Song, E., Bandfield, J. L., Lucey, P. G., Greenhagen, B. T., & Paige, D. A. (2013). Bulk mineralogy of lunar crater central peaks via thermal infrared spectra from the Diviner Lunar Radiometer: A study of the Moon's crustal composition at depth. *Journal of Geophysical Research: Planets*, *118*, 689–707. https://doi.org/10.1002/jgre.20065
Staid, M. I. (2000). Remote determination of the mineralogy and optical alteration of lunar basalts using clementine multispectral images: Global comparisons of mare volcanism (PhD Thesis). Brown University.
Sunshine, J. M., & Pieters, C. M. (1998). Determining the composition of olivine from reflectance spectroscopy. *Journal of Geophysical Research*, *103*, 675–688.
Thorey, C., Michaut, C., & Wieczorek, M. (2015). Gravitational signatures of lunar floor-fractured craters. *Earth and Planetary Science Letters*, *1*, 1–11. https://doi.org/10.1016/j.epsl.2015.04.021
Tompkins, S., & Pieters, C. M. (1999). Mineralogy of the lunar crust: Results from Clementine. *Meteoritics & Planetary Science*, *34*, 25–41.
Tompkins, S., & Pieters, C. M. (2010). Spectral characteristics of lunar impact melts and inferred mineralogy. *Meteoritics and Planetary Science*, *45*(7), 1152–1169. https://doi.org/10.1111/j.1945-5100.2010.01074.x
Vaughan, W. M., Head, J. W., Wilson, L., & Hess, P. C. (2013). Geology and petrology of enormous volumes of impact melt on the Moon: A case study of the Orientale basin impact melt sea. *Icarus*, *223*(2), 749–765. https://doi.org/10.1016/j.icarus.2013.01.017
Warren, P. H. (1985). The magma ocean concept and lunar evolution. *Annual Review of Earth and Planetary Science*, *13*, 201–40. https://doi.org/10.1146/annurev.earth.13.1.201
Wieczorek, M. A., Neumann, G. A., Nimmo, F., Kiefer, W. S., Taylor, G. J., Melosh, H. J., … Zuber, M. T. (2013). The crust of the Moon as seen by GRAIL. *Science (New York N.Y.)*, *339*(6120), 671–675. https://doi.org/10.1126/science.1231530
Wieczorek, M. A., & Zuber, M. T. (2001). The composition and origin of the lunar crust: Constraints from central peaks and crustal thickness modeling. *Geophysical Research Letters*, *28*(21), 4023–4026. https://doi.org/10.1029/2001GL012918
Wilhelms, D. E., & El-Baz, F. (1977). Geological Map of the East Side of the Moon.
Wilhelms, D. E., McCauley, J. F., & Trask, N. J. (1987). The geologic history of the moon (Professional Paper 1348).
Yamamoto, S., Nakamura, R., Matsunaga, T., Ogawa, Y., Ishihara, Y., Morota, T., … Haruyama, J. (2010). Possible mantle origin of olivine around lunar impact basins detected by SELENE. *Nature Geoscience*, *3*(8), 533–536. https://doi.org/10.1038/ngeo897